International Journal of Fracture **100:** 275–306, 1999.

Compressive response and failure of fiber reinforced unidirectional composites

S.H. LEE* and ANTHONY M. WAAS**
University of Michigan, Department of Aerospace Engineering, MI 48109-2140, Ann Arbor, U.S.A.

Received 28 December, 1998; accepted in revised form 15 July 1999

Abstract. The compressive response of polymer matrix fiber reinforced unidirectional composites (PMC's) is investigated via a combination of experiment and analysis. The study accounts for the nonlinear constitutive response of the polymer matrix material and examines the effect of fiber geometric imperfections, fiber mechanical properties and fiber volume fraction on the measured compressive strength and compressive failure mechanism. Glass and carbon fiber reinforced unidirectional composite specimens are manufactured in-house with fiber volume fractions ranging over $10 \sim 60$ percent. Compression test results with these specimens show that carbon fiber composites have lower compressive strengths than glass fiber composites. Glass fiber composites demonstrate a splitting failure mode for a range of low fiber volume fractions and a simultaneous splitting/kink banding failure mode for high fiber volume fractions. Carbon fiber composites show kink banding throughout the range of fiber volume fractions examined. Nonlinear material properties of the matrix, orthotropic material properties of the carbon fiber, initial geometric fiber imperfections and nonuniform fiber volume fraction are all included in an appropriate finite element analysis to explain some of the observed experimental results. A new analytical model prediction of the splitting failure mode shows that this failure mode is favorable for glass fiber composites, which is in agreement with test results. Furthermore, this model is able to show the influence of fiber mechanical properties, fiber volume fraction and fiber geometry on the splitting failure mode.

Key words: Kink banding, splitting, compression strength, fracture.

1. Introduction

It is established that the compressive strength of PMC's is generally lower than the tensile strength; this relative weakness in compression is often the limiting factor in the application of composite materials. In order to design a composite structure to operate efficiently and safely under compressive loading, it is necessary to be able to accurately predict the compressive strength of that structure, taking into account the possible failure modes of the structure under different conditions.

A significant number of previous experimental results have revealed that material failure (usually at the microstructural level) such as fiber microbuckling or kinking in laminae where the fibers are aligned with the loading axis are the initiating mechanisms of compressive failure that lead to global instability (Sohi et al., 1987; Waas et al., 1990; Soutis et al., 1991), in composite structures. There is, thus, a necessity to develop a means of measuring the strength of a lamina (derived from a test of a structure with the fibers aligned with the load), which can be coupled with measured strengths in other orientations in an appropriate failure model, such as those described in Cui et al. (1992). This failure model can then be used in conjunction

* Graduate Research Assistant. Now at GM Technical Center, Warren, MI.
** Associate Professor. Author to whom all correspondence should be addressed. e-mail: dcw@umich.edu.

with the laminate layup and the stress and strain distributions calculated from models using CLT type theories to predict failure of the structure based on its construction.

Compression failure in composites is an area of active research, and other sources of information on this topic are presented in recent review articles by Schoeppner and Sierakowski (1990), Camponeschi (1991), Guynn et al. (1992), Lo and Chim (1992), Chatterjee et al. (1993), Waas and Schultheisz (1995) and Fleck (1997). The reviews by Waas and Schultheisz (1995) and Fleck (1997) are the most up-to date and examines issues related to compressive failure rather exhaustively. The papers by Budiansky and Fleck (1993) and Kyriakides et al. (1995), provides a thorough treatment of plastic microbuckling and the initiation and localization of deformation into kink bands, respectively. Since the publication of the above articles, important contributions by Daniel (1996), who examined manufacturing process induced defects and rate effects on compression strength, Sun and Jun (1994), who used a lamina level plasticity formulation and Schapery (1993, 1995) who examines time dependent microbuckling failure have also appeared. In addition, Shu and Fleck (1997) have used a couple stress theory to examine microbuckling, while the effects of other plies on the zero ply microbuckling strength of laminates have been examined by Swanson (1992) and Drapier et al. (1998). Free edge effects and three-dimensional corrections have also been studied by Soutis et al. (1998) and Kyriakides and Ruff (1997) respectively. Narayan and Schadler (1998), have proposed a new mechanism for the initiation of kink banding based on experiments with unidirectional composites in conjunction with Raman Spectroscopy. They propose a model based on the development of a distributed damage zone due to fiber end effects.

The most frequently considered failure modes in unidirectional laminates are microbuckling, kinking, fiber failure and longitudinal cracking (synonymous with delamination failure in general laminates). Obviously, these failure modes may combine in any one specimen, or a different mode may dominate for the same composite material tested under different conditions. The test method itself may influence the measured compressive strength, particularly if the testing apparatus induces stress concentrations or does not prevent global buckling of the structure. Thus, the term compressive strength has meaning only if the mode of failure associated with the strength measurement is specified.

The present paper is concerned with an exploration of the parameters that influence compressive strength of unidirectional composites. The effect of adjacent plies and their location with respect to zero plies, on the compressive strength of multidirectional laminates is not explored herein. Of concern in the present work is how the mechanism of failure in compressively loaded unidirectional composites is influenced by the mechanical properties of the fiber, the fiber volume fraction and nonuniform packing of the fibers. A case is made for the importance of performing a mechanism based failure analysis of the composites. In the sections to follow, we begin with an exposition of the experimental work, followed by a new analytical model for explaining the splitting failure mode of composites and a finite element analysis of the observed kink band failure mode. A discussion ensues as to how these mechanisms are related. A comprehensive and detailed version of the present work is contained in the doctoral thesis of the first author (Lee, 1998).

2. Experiments

Uni-directional composite specimens were made in-house for static compression tests. Two different kinds of fibers (glass and carbon) were used for specimens, while only one type of

matrix material (vinyl ester resin) was used as the matrix. Such an approach enabled us to examine the effect of fiber mechanical property on the compressive behavior of unidirectional composites. The fiber volume fraction of the specimens could be easily controlled during the manufacturing process used in this investigation. Specimens with six different volume fractions were manufactured.

The making of the specimens involved taking an exact amount of fibers (without any fiber surface treatment) matching the desired fiber volume fraction, which was put inside a glass tube with an internal diameter of 6.8 mm and 300 mm length. Next, resin mixed with 1 percent weight of initiator (Benzoyl Peroxide), was injected into the glass tube under pressure of 70–140 Pa. The resin was circulated in the glass tube so that all the fibers were adequately wetted, which resulted in a void free composite sample. After the tubes were filled, they were placed in a furnace and cured at 80°C for 2 hours. After cooling to room temperature, the specimens were cut by a diamond saw, which resulted in a flat and smooth cutting section.

The two types of fiber materials used for the specimens were E-glass fiber of 24.1 μm diameter (Certainteed R099-625 E-glass fiber) and Carbon fiber of 5 μm diameter (Hercules IM-7-12K). The matrix material used for specimens was a vinyl ester resin (Dow Derakane 411-C50).

2.1. Compression tests

Compression tests were performed in a hydraulically actuated loading frame. The specimens of length 63.5 mm were fit into grips which have a 25.4 mm length and a slightly larger than 6.4 mm circular opening. The gage length of the specimen was 12.7 mm. When the specimens were compressed, the grips were restrained from moving laterally. The tests were performed under displacement control with a cross head speed of 0.0381 mm/sec. Loads were measured by a load cell at the top of the specimen. Back-to-back strain gages were attached at the center of the specimen in the longitudinal direction to measure the compressive strain and any bending strain. A schematic of the test set-up used for the static compression tests of uni-directional composites is shown in Figure 1. The test specimens used are short enough that global Euler buckling is prevented. In addition, any effects caused by stress concentration at the grips are deemed negligible due to the fact that repeatable failure was observed in the gage section for all of the glass fiber composites. For carbon fiber composites, the lateral constraint provided by the grips leads to failure by kink banding, occurring inside the grips (away from the load introduction end faces and also away from the grip termination location). This aspect of failure initiation in carbon fiber composites is discussed later.

A total of 46 specimens were tested. The breakdown is as follows: 3 of the pure resin specimens, 21 of glass fiber reinforced specimens (3 each of 10, 20, 30 percent volume fractions, 4 each of 40, 50, 60 percent volume fractions) and 22 of carbon fiber reinforced specimens (3 each of 10, 20, 30, 40 percent volume fractions, 6 of 50, 4 of 60 percent volume fractions).

2.2. Test results

From the compression tests, the axial stress-strain response (referred to as the σ–ε curve) of the uni-directional glass and carbon fiber reinforced vinyl ester resin composites was obtained as a function of the fiber volume fraction. Important mechanical properties of the composites were deduced from the σ–ε curves. The Young's modulus of the pure resin material was measured as 3,693 MPa from the compression test of the pure resin specimens. Using this

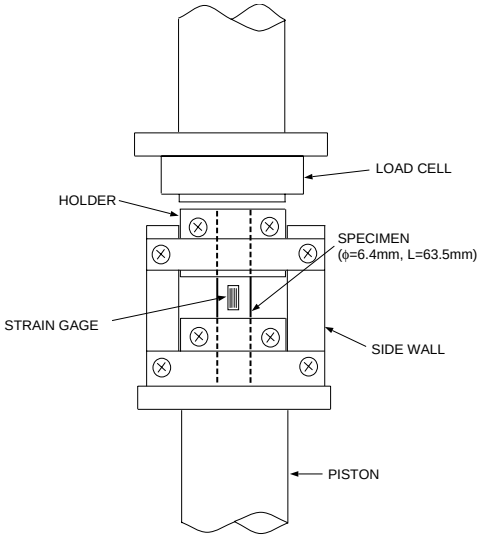

Figure 1. Schematic of the compression test set-up.

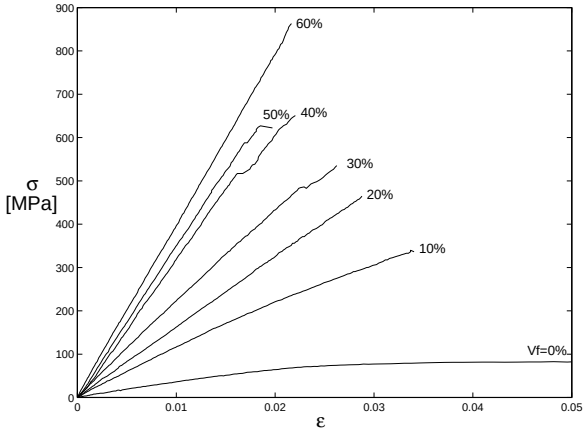

Figure 2. Typical compressive stress-strain curves of glass-fiber composites.

value, the stiffness of the composite material in the axial direction, E_{11}, was calculated via the rule of mixtures (E-glass fiber: $E = 72\,\text{GPa}$ (Kumar, 1991), Carbon fiber: $E = 276\,\text{GPa}$ (Guynn et al., 1992b; Jones, 1975)). E_{11} measured in each compression test was compared to the rule of mixture result. The experimental result was approximately $83 \sim 107$ percent of the rule of mixture prediction. Typical σ–ε curves of glass fiber composites throughout the volume fraction range $10 \sim 60$ percent is shown in Figure 2. From these curves, the compressive strength and the axial stiffnesses of the composites are obtained.

A typical σ–ε curve of a carbon fiber composite is shown in Figure 3 for the case corresponding to a fiber volume fraction 10 percent. The σ–ε curve is very irregular, because the carbon fiber composite fails in a progressive manner, quite different from the catastrophic failure of the glass fiber composites. The carbon fiber composites fail by kink band development during the test. This phenomenon can be clearly understood by examining a stress-time curve as shown in Figure 4 and an examination of the specimen after the test as shown in

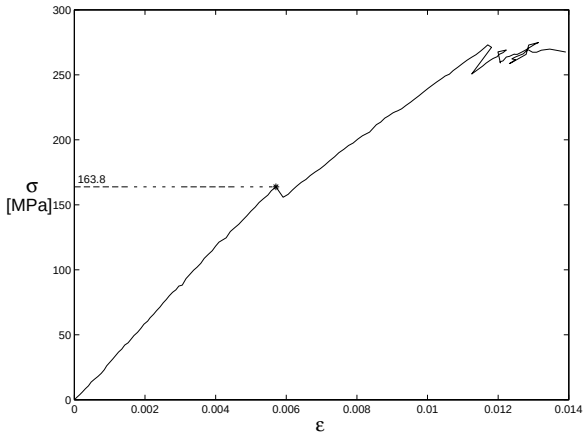

Figure 3. Typical compressive stress-strain curve of a carbon-fiber composite specimen, ($V_f = 10$ percent).

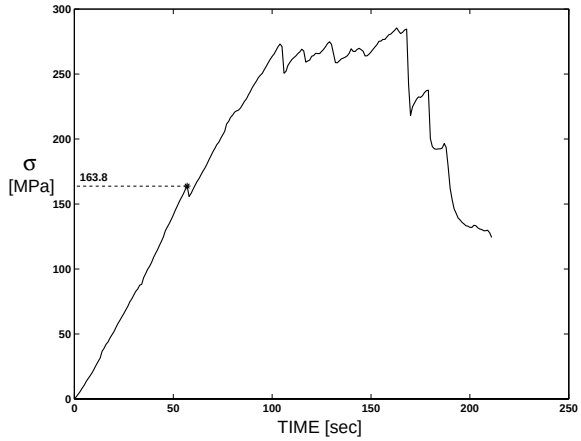

Figure 4. Typical compressive stress-time curve of a carbon-fiber composite specimen, ($V_f = 10$ percent).

Figure 5. When a kink band is formed, there is a sudden load drop and the strain changes at the location at which the strain gage is mounted. In fact, the initial kink band usually develops inside the constrained grip section of the sample, as a result, the axial strain in the gage section relaxes as indicated by the recorded strain gage output. Further loading leads to an increase in load until the next kink band forms and this sequence of events is found to repeat itself. The resulting stress-time curves, stress-strain curves and post experiment photomicrographs add confirmation to these findings. Similar experimental results were obtained for specimens with V_f ranging from 10–60 percent. Unlike glass fiber composites, the maximum strength of the carbon fiber composites does not show a well defined trend. The maximum strength of the composite in the case of kink banding is determined by the first load drop corresponding to the formation of the first kink band as shown in the stress-time curve depicted in Figure 4.

The unloaded and failed composite specimens were inspected under an optical microscope after the tests. Typical optical micrographs are shown in Figure 5 through Figure 9. It is seen that fibers are randomly located in the composite. A longitudinal section of a carbon fiber

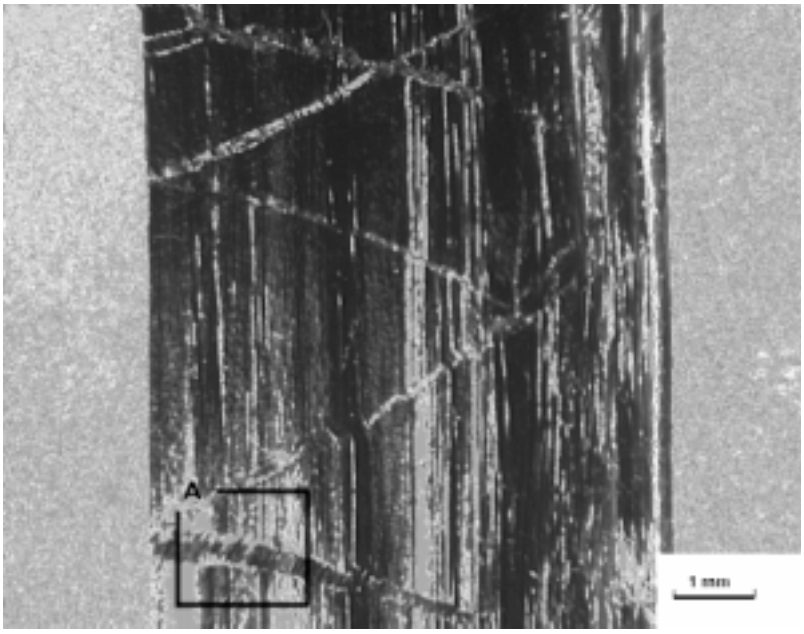

Figure 5. Typical kink band failure mode of a carbon fiber composite specimen, ($V_f = 10$ percent).

composite with $V_f = 10$ percent is shown in Figure 6. From this longitudinal cross section of the composite, the fiber misalignment angle ϕ is measured and is found to be less than 3°. On average, a typical number for the misalignment was 2°, for the specimens studied herein. The sections obtained after the specimens were subjected to failure are shown in Figure 7 through Figure 9. Glass fiber specimens show a splitting mode of failure (sometimes also referred to as 'brooming' in the literature) as shown in Figure 7. The fiber/matrix interfaces split during the test and the fibers are broken during the process of failure. For high fiber volume fractions (40 $\sim$ 60 percent), kink bands are also observed (Figure 8). It is postulated that these kink bands are formed on account of the synergy due to the misalignment induced during the axial splitting and the large amount of strain energy that is released. Indeed, in the glass fiber composites, isolated kink bands were never observed. When kink bands were found they were always accompanied by longitudinal fiber/matrix splitting cracks. It is, however, quite possible that kinking in conjunction with a low interfacial fracture toughness can induce axial splits. A comparison of the experimentally measured compressive strength of glass fiber composites and carbon fiber composites is shown in Figure 10.

In summary, the experimental results show that glass fiber composites fail by splitting which is the predominant mode of failure of these composites in the 10 $\sim$ 30 percent fiber volume fraction range. For glass fiber composites with 40 $\sim$ 60 percent fiber volume fraction, both splitting and kink banding are observed. However the formation of kink bands is not progressive (signified by a clear drop in load) as in carbon fiber composites, but, leads to catastrophic failure via axial splitting. Throughout the entire range of fiber volume fraction (10 $\sim$ 60 percent), the carbon fiber composites fail by kink banding as shown in the photomicrographs of Figure 5 and Figure 9. The kink bands are well defined and they form in a progressive manner, starting from the specimen area that is confined within the grips. Similar results for a different carbon fiber system (AS4/PEEK) have been reported by Kyriakides et al. (1995). Even for the low fiber volume fraction range (10 $\sim$ 30 percent), the splitting

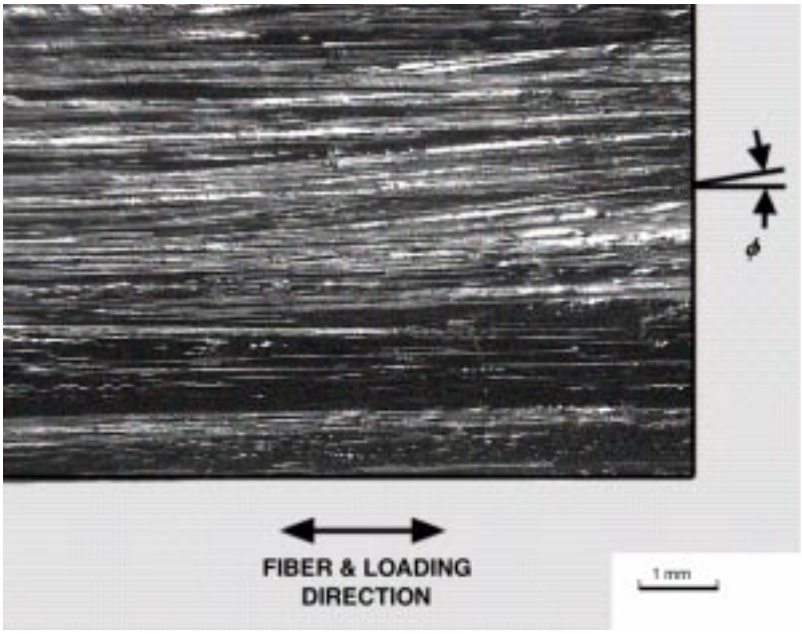

Figure 6. Typical longitudinal cross section of a composite specimen (Carbon fiber, $V_f = 10$ percent).

failure mode that was dominant for the glass fiber composites was absent in the carbon fiber composites. These results show that the compression response and failure of a composite is strongly influenced by the mechanical properties of the fiber, the geometry of the fibers (fiber diameter), the fiber volume fraction and possibly the quality of the interface between the fiber and matrix. In the present case both glass and carbon fibers were untreated prior to manufacturing of the specimens and thus the nature of the interfacial fiber/matrix bond is dictated by the chemistry between glass/vinyl ester and carbon/vinyl ester. The implications of the experimental findings that have been presented are examined next via a new analytical model for the splitting failure mode and a numerical analysis for the kink banding failure mode.

3. Splitting

The splitting failure mode is hypothesized to occur when a pre-existing flaw inside the specimen starts to grow when the specimen is under compression load. The splitting failure mode was predominant for the glass fiber composites. Yet, it was noticeably absent in the carbon fiber composites. Because the splitting failure is hypothesized to initiate from tiny unavoidable flaws within the composite, the compressive strength of the composite specimens are closely related to the appropriate crack toughnesses $K_{\mathrm{I}C}$ and/or $K_{\mathrm{II}C}$. The worst case scenario would be for a flaw at the interface between a fiber and a matrix in which case K_{IC} and $K_{\mathrm{II}C}$ would be the opening and sliding mode toughnesses corresponding to fiber/matrix interface failure. During the process of manufacturing composite specimens, it is reasonable to expect that they might contain tiny internal cracks. It is relatively easy to contemplate that the fiber/matrix interface has a crack (caused by nonwetting) during the curing process. In the present study, a representative volume element (RVE) that consists of a single fiber in a matrix cylinder and containing a central interface crack is considered. The outer radius of the matrix cylinder is

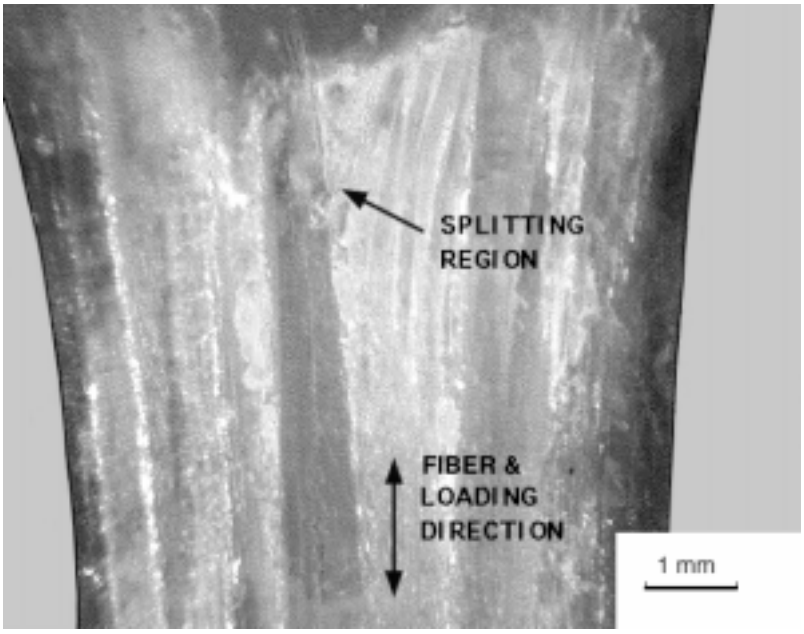

Figure 7. Typical splitting failure mode of glass fiber composites, ($V_f = 30$ percent).

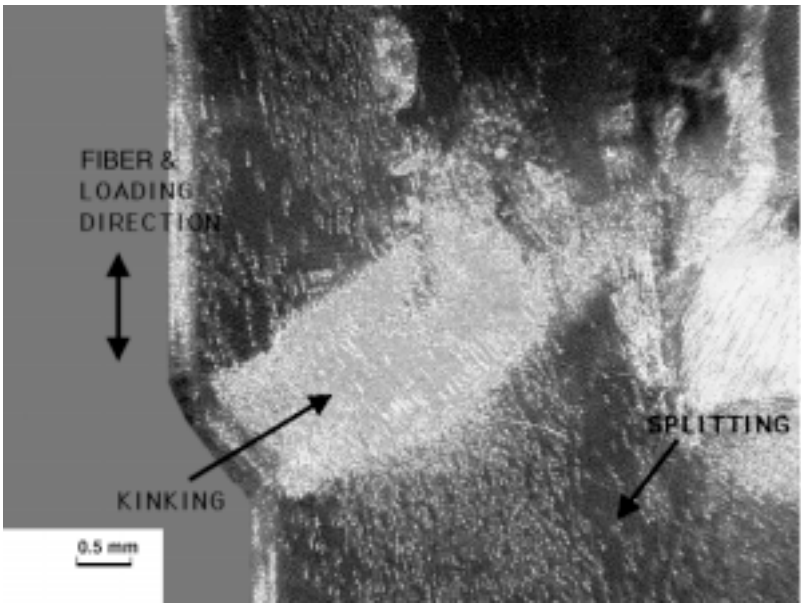

Figure 8. Typical splitting/kinking failure mode of glass fiber composite, ($V_f = 40$ percent).

chosen to match the fiber volume fraction of the corresponding composite. An examination of the total potential energy in conjunction with principles of linear elastic fracture mechanics is next used to predict the compressive load at which crack propagation occurs. Since the fibers within the composite can have an initial misalignment with respect to axial load, the influence of such fiber crookedness is also incorporated in the development of the splitting model. The latter is presented in Section 3.1.1. It is noted that Cherepanov (1979), used a

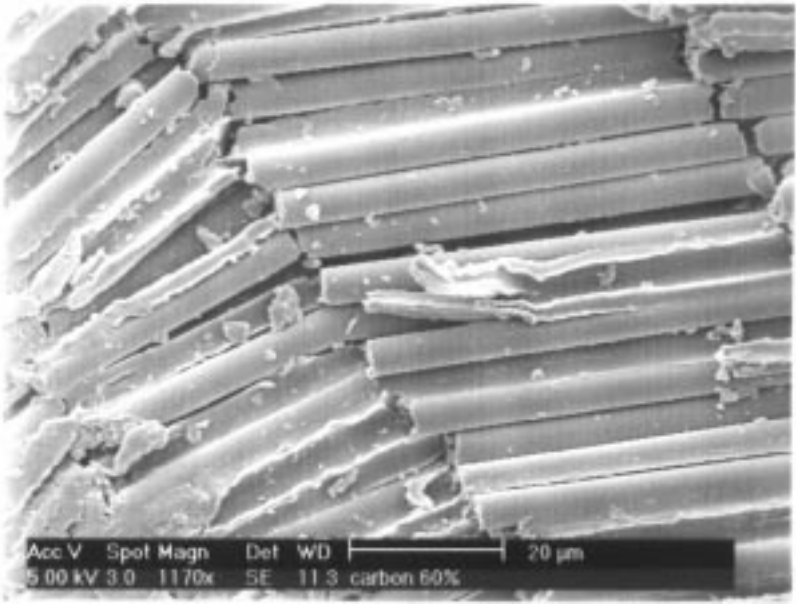

Figure 9. A close up of the kinking failure mode of carbon fiber composite, ($V_f = 60$ percent).

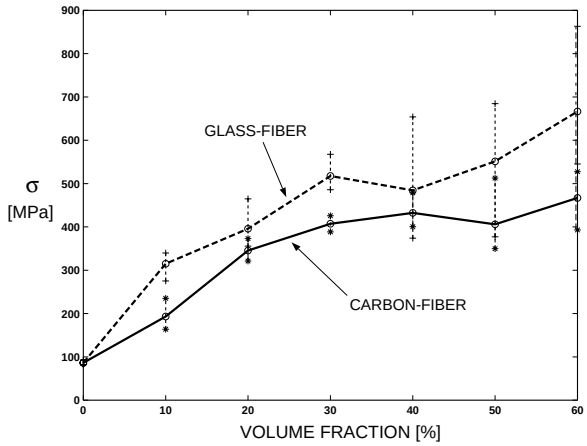

Figure 10. Maximum stress as a function of fiber volume fraction.

conserved T-integral approach to arrive at an expression for axial splitting. The approach we have taken differs in that an expression is first obtained for the steady state energy release rate by using ideas from classical fracture mechanics. This energy release rate is next compared with the interfacial fracture energy to determine the load envelope corresponding to fracture propagation. Both, perfectly aligned and misaligned fibers are considered. In addition, an axisymmetric finite element analysis is carried out for short interfacial cracks, where the energy release rate is found to be dependent on the crack length.

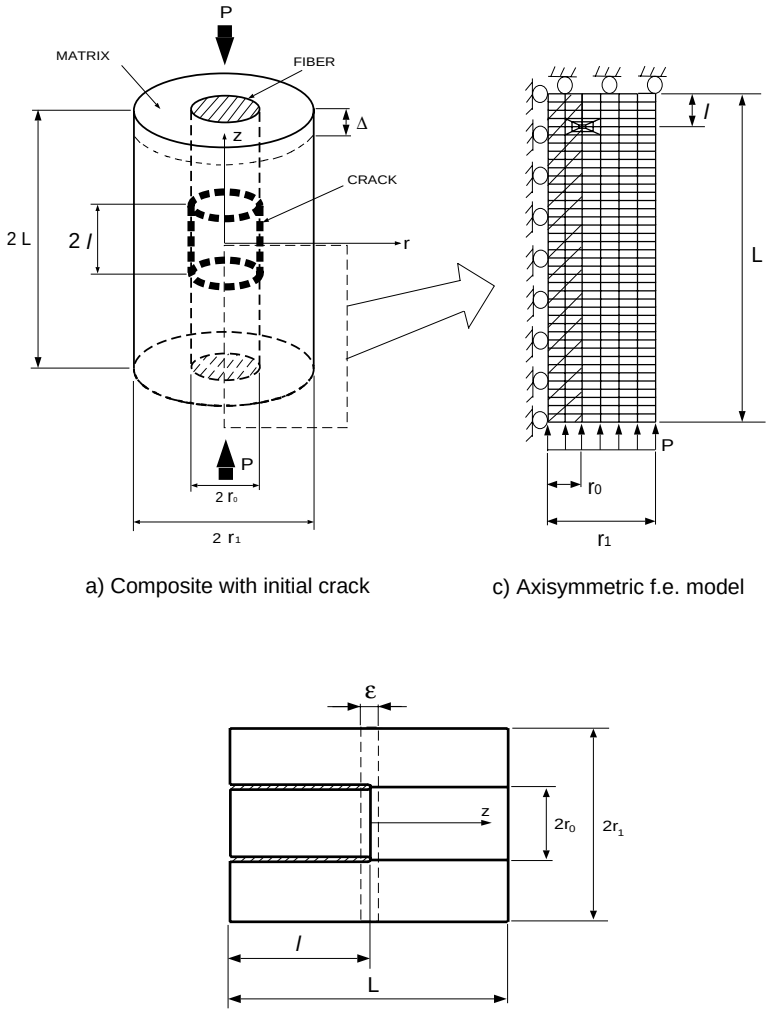

Figure 11. Composite model for splitting failure, with an initial interface crack.

3.1. ANALYSIS

Consider a RVE of a unidirectional composite of length $2L$, which has a fiber/matrix interface crack of length $2l$ as shown in Figure 11(a). The fiber/matrix cylinder is compressed by an external load P as indicated. The outer radius of the matrix is chosen such that the RVE has the same fiber volume fraction as the composite. Thus, $r_0^2 = V_f r_1^2$. Further, the outer matrix surface ($r = r_1$) is assumed traction free. In the RVE, the fiber occupies the region, $r \leqslant r_0$ and the matrix occupies the region, $r_0 \leqslant r \leqslant r_1$. Along the crack surface, $(-l \leqslant z \leqslant l, r = r_0)$, the fiber is not bonded to the matrix, while outside this region, perfect bonding between fiber and matrix is assumed. The total potential energy is $\Pi = U - W$, where U is strain energy and W is the work done.

The energy release rate is defined as

$$G = -\frac{\mathrm{d}\Pi}{\mathrm{d}A},$$

where $A = 4\pi r_0 l$ is the crack surface area.

The compliance c is defined as

$$c = \frac{\Delta}{P},$$

where Δ is the axial compressive deflection of the composite and P is the external compressive load.

For the case of load control (P is held constant during crack propagation)

$$\begin{aligned} W &= P\Delta, \\ U &= \tfrac{1}{2}P\Delta, \\ \Pi &= -\tfrac{1}{2}P\Delta, \\ G &= \frac{P^2}{8\pi r_0}\frac{\mathrm{d}c}{\mathrm{d}l}, \end{aligned}$$

while for displacement control (Δ is held constant during crack propagation):

$$\begin{aligned} W &= 0, \\ U &= \tfrac{1}{2}P\Delta, \\ \Pi &= \tfrac{1}{2}P\Delta, \\ G &= \frac{P^2}{8\pi r_0}\frac{\mathrm{d}c}{\mathrm{d}l}. \end{aligned}$$

Notice that the expression for G is the same for load control and displacement control, because of the assumption of linear elastic material behavior.

For the cracked region in Figure 11(a) ($-l \leqslant z \leqslant l$), the stress state which corresponds to axial compression is given as follows (Lee, 1998).

Fiber:

$$\sigma_z = \frac{PE_f}{\pi r_0^2 \delta}.$$

Matrix:

$$\sigma_z = \frac{PE_m}{\pi r_0^2 \delta},$$

where

$$\delta = E_f + E_m\left(\frac{1}{V_f} - 1\right).$$

All other stresses are zero.

The axial contraction of the fiber and matrix in the cracked region can be obtained from the axial strain corresponding to the above stresses, and is given by

$$\Delta_1 = \int_{-l}^{l} \varepsilon_z \, \mathrm{d}z = \frac{2Pl}{\pi r_0^2 \delta}.$$

For the uncracked region in Figure 11(a) ($l \leqslant z \leqslant L, -L \leqslant z \leqslant -l$), the stress state which is three dimensional, is given as follows (Lee, 1998).

Fiber:

$$\sigma_r = \sigma_\theta = \frac{2P}{\pi r_0^2}\alpha\beta(\nu_f - \nu_m)(V_f^{-1} - 1),$$

$$\sigma_z = \frac{\beta P}{\pi r_0^2}[E_f + 4\alpha\nu_f(\nu_f - \nu_m)(V_f^{-1} - 1)].$$

Matrix:

$$\sigma_r = 2\alpha\beta P \frac{\nu_f - \nu_m}{\pi r_0^2}\left(\frac{r_0^2}{r^2 V_f} - 1\right),$$

$$\sigma_\theta = -2\alpha\beta P \frac{\nu_f - \nu_m}{\pi r_0^2}\left(\frac{r_0^2}{r^2 V_f} + 1\right),$$

$$\sigma_z = \frac{\beta P}{\pi r_0^2}\left[E_m - 4\alpha\nu_m(\nu_f - \nu_m)\right],$$

where

$$\alpha = \left[\frac{2(1+\nu_f)(1-2\nu_f)}{E_f}(V_f^{-1} - 1) + \frac{2(1+\nu_m)(1-2\nu_m + V_f^{-1})}{E_m}\right]^{-1},$$

$$\beta = \left[E_f + (V_f^{-1} - 1)\{E_m + 4\alpha(\nu_f - \nu_m)^2\}\right]^{-1}.$$

The axial strains corresponding to these stresses are as follows.

Fiber:

$$\varepsilon_z = -\frac{\nu_f}{E_f}\sigma_r - \frac{\nu_f}{E_f}\sigma_\theta + \frac{1}{E_f}\sigma_z$$

$$= -\frac{4P\nu_f}{\pi r_0^2 E_f}\alpha\beta(\nu_f - \nu_m)(V_f^{-1} - 1)$$

$$+\frac{\beta P}{\pi r_0^2 E_f}[E_f + 4\alpha\nu_f(\nu_f - \nu_m)(V_f^{-1} - 1)].$$

Matrix:

$$\varepsilon_z = \frac{4\alpha\beta P\nu_m(\nu_f - \nu_m)}{\pi r_0^2 E_m} + \frac{\beta P}{\pi r_0^2 E_m}[E_m - 4\alpha\nu_m(\nu_f - \nu_m)].$$

The axial contraction of the fiber and matrix are the same in this region and is given by

$$\Delta_2 = 2\int_l^L \varepsilon_z \, \mathrm{d}z = \frac{2\beta P}{\pi r_0^2}(L-l).$$

Hence, the approximate total axial contraction, approximate compliance and change of compliance with respect to crack length of the composite are as follows.

$$\Delta = \frac{2P}{\pi r_0^2}\left[\frac{l}{\delta} + \beta(L-l)\right],$$

$$c = \frac{2}{\pi r_0^2}\left[\frac{l}{\delta} + \beta(L-l)\right],$$

$$\frac{\mathrm{d}c}{\mathrm{d}l} = \frac{2}{\pi r_0^2}\left(\frac{1}{\delta} - \beta\right).$$

In computing the above quantities, only the stress states of the cracked and uncracked regions are considered, whereas a region near the crack tip of finite size ε is not considered. In this region (Figure 11(b)), the stress state is influenced by the crack tip field. However, when the crack propagates under steady state conditions, this region translates with the crack tip resulting in an increase of l and a corresponding decrease of $(L-l)$. Thus, while the axial contraction and compliance given by Δ and c above are subject to a minor error due to the negligence of the crack tip field, the rate of compliance change due to crack advancement, given by $\mathrm{d}c/\mathrm{d}l$ is exact, since the 'ε' region is invariant with respect to crack length. This fact enables us to calculate G accurately for steady state crack propagation.

Finally, the energy release rate per unit area is obtained from the above quantities as

$$G = \frac{P^2}{4\pi^2 r_0^3}\left(\frac{1}{\delta} - \beta\right).$$

When this energy release rate per unit area, G, becomes equal to twice the critical interfacial surface energy (γ_f) the initial crack propagates

$$G = 2\gamma_f.$$

3.1.1. *Misaligned fibers*

The expression for axial compliance for the case when the fiber is misaligned in the cracked region can be obtained by considering a slightly imperfect fiber with an initial imperfection of $w_0(x)$ and using kinematics that are appropriate for geometrically nonlinear beam theory as described in Appendix B. Then the relation between axial contraction Δ_1, and fiber load P_f can be obtained as,

$$\frac{\Delta_1}{l} = \frac{-P_f}{A_f E_f}\left[1 + \frac{A_0^2 A_f}{2I_f}\right],$$

where, A_f is the fiber cross-sectional area, I_f is the fiber area moment of inertia and A_0 is the imperfection magnitude. From this relation an effective axial stiffness for the fiber is obtained and is given below

$$(EA)_{\text{eff}} = \frac{E_f A_f}{1 + \frac{A_0^2 A_f}{2I_f}}.$$

Clearly, when the imperfection vanishes, one recovers the perfect fiber axial stiffness $E_f A_f$. In the present work, the imperfection amplitude is chosen to correspond to an initial misalignment angle of 2°, representative of what was measured in the experiment.

Splitting failure was dominant for the low volume fraction glass fiber composites. Thus, the test data from the 10–20 percent volume fraction glass fiber composites provide us a means to obtain the interfacial toughness γ_f, for a glass/vinyl ester interface, corresponding to the two splitting models (perfectly aligned and misaligned fibers, respectively). In so doing, the range of γ_f obtained are $1.0546 \times 10^{-4}\,\mathrm{KJ/m^2}$ to $3.9357 \times 10^{-5}\,\mathrm{KJ/m^2}$, for the perfectly aligned case and $0.1224\,\mathrm{KJ/m^2}$ to $0.083\,\mathrm{KJ/m^2}$, for the misaligned case. Such an approach to obtain γ_f was used because we are interested in obtaining a measure of fracture toughness that is related to the total energy release rate, without explicitly considering the component modes of energy release rates. If one performs suitable double cantilever tests or end notch flexure tests, then component modes of toughness can be measured, however, their use in an appropriate analytical model is not so straightforward. The values obtained for γ_f as noted above are in the range of fracture toughnesses for polymers as reported in Ashby (1992), and are acceptable as reasonable interfacial adhesive toughness values for a glass/vinyl ester system. Both these ranges are used in comparing the model predictions with the experimental data.

Critical splitting stresses for glass fiber composites corresponding to the above range of toughnesses are shown in Figures 12 and 13 respectively. Corresponding resultant critical stresses for carbon fiber composites using the same values of γ_f are shown in Figures 14 and 15, respectively. Notice that, we used the same values of interfacial toughnesses for the carbon/vinyl ester interface, although this value should be probably higher. Even then, the critical stresses required to split a carbon fiber composite, based on the γ_f corresponding to a glass/vinyl ester interface is still much larger than that required to cause kinking. This is because the carbon fiber has a larger modulus and a smaller radius than the glass fiber. In effect, our splitting model shows that the axial stiffness ratio between fiber to matrix, the fiber volume fraction, the fiber diameter and the interfacial fracture toughness are all important parameters that dictate splitting failure in a compressively loaded composite, just as misalignment and matrix yield strength are for compressive kinking. To the best knowledge of the authors, a model for compressive splitting failure in conjunction with discussions on composite compressive strength have not been reported before.

3.2. Axisymmetric finite element model for short cracks

The steady state expression for the energy release rate G, in the previous section does not include the initial crack length ($2l$) nor the composite length ($2L$). For short (compared to the fiber radius) cracks, it becomes necessary to use the finite element method to extract the dependency of crack length on G. Axisymmetric finite element models as shown in Figure 11(c) were used in simulating one half of the glass fiber composites corresponding to the extremes of $V_f = 10$ and 60 percent with fixed composite length $L = 0.241\,\mathrm{mm}$ and various crack lengths in the range $0\,\mathrm{mm} \leqslant l \leqslant 0.0723\,\mathrm{mm}$. After applying a prescribed compressive load to cause a uniform axial deflection, the compliance $c = \Delta/P$ was calculated. Only the case of perfectly aligned fibers was analyzed with the intent of lending credence to the steady state result obtained earlier.

The compliances as a function of crack length obtained from the finite element method show linear ranges beyond a certain crack length for both the $V_f = 10$ and 60 percent cases as shown in Figures 16 and 17. The rate of change of compliance with respect to

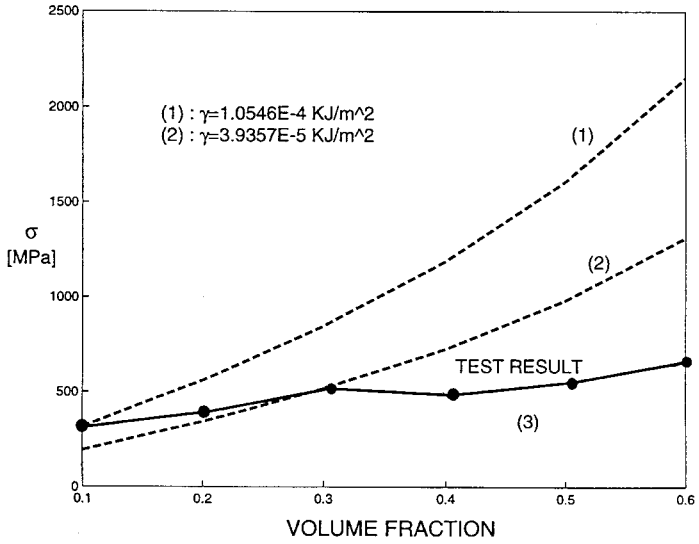

Figure 12. Predictions of the splitting model for glass fiber composites; perfect fibers..

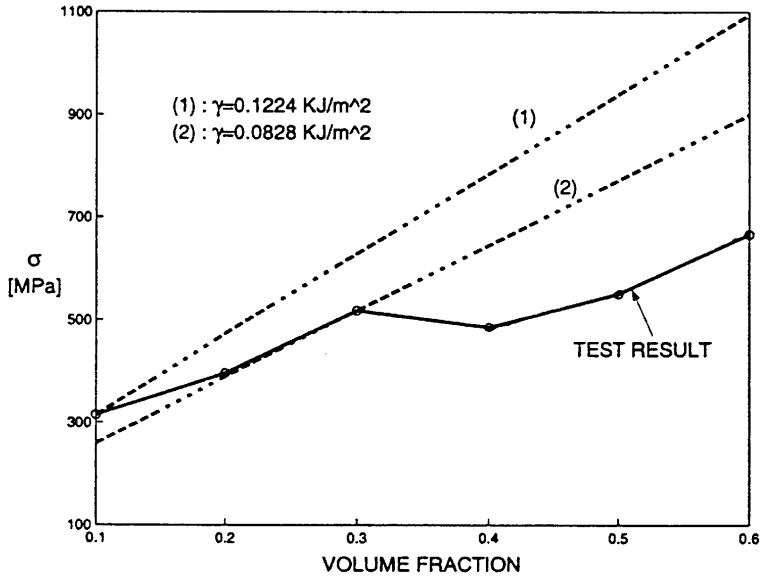

Figure 13. Predictions of the splitting model for glass fiber composites; imperfect fibers.

crack length $\mathrm{d}c/\mathrm{d}l$, obtained from the analysis (steady state) and the finite element model are listed in Table 1. For the $V_f = 10$ percent model, $\mathrm{d}c/\mathrm{d}l = 3.1881 \times 10^{-5}\,\mathrm{N}^{-1}$ beyond $l/L = 0.075$. This value is approximately the same as $\mathrm{d}c/\mathrm{d}l = 3.0937 \times 10^{-5}\,\mathrm{N}^{-1}$ obtained from the analytical steady state solution (the difference is 3 percent). For the $V_f = 60$ percent model, $\mathrm{d}c/\mathrm{d}l = 2.4042 \times 10^{-5}\,\mathrm{N}^{-1}$ beyond $l/L = 0.015$. This is very close to the value of $\mathrm{d}c/\mathrm{d}l = 2.3969 \times 10^{-5}\,\mathrm{N}^{-1}$ obtained from the analytical solution (difference is 0.3 percent). Thus, these limit cases add further confirmation to the veracity of the proposed splitting model.

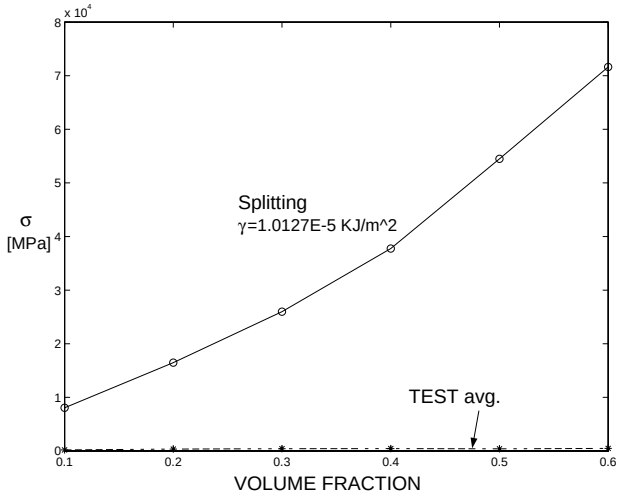

Figure 14. Predictions of the splitting model for carbon fiber composites; perfect fibers.

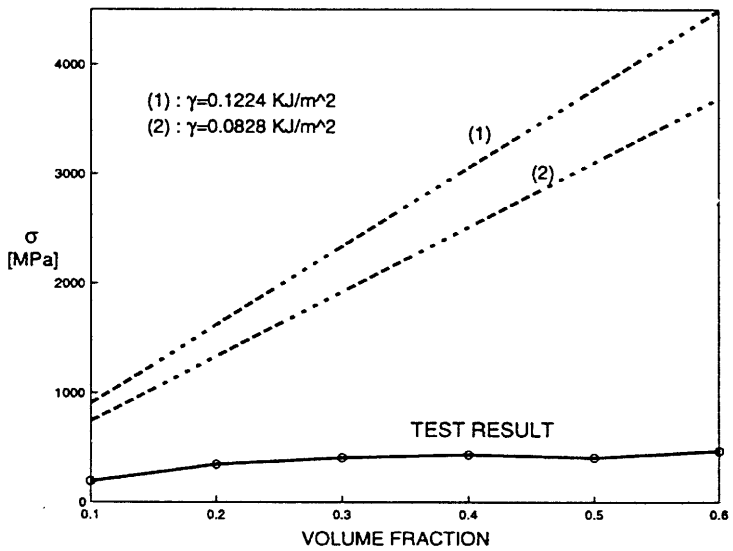

Figure 15. Predictions of the splitting model for carbon fiber composites; imperfect fibers.

Table 1. Rate of change of compliance, $(\mathrm{d}c/\mathrm{d}l[\mathrm{N}^{-1}]$ of glass fiber composites.

V_f[%]	Analysis	F.E.M.	Difference [%]
10	3.0937×10^{-5}	3.1881×10^{-5}	3.1
60	2.3969×10^{-5}	2.4042×10^{-5}	0.3

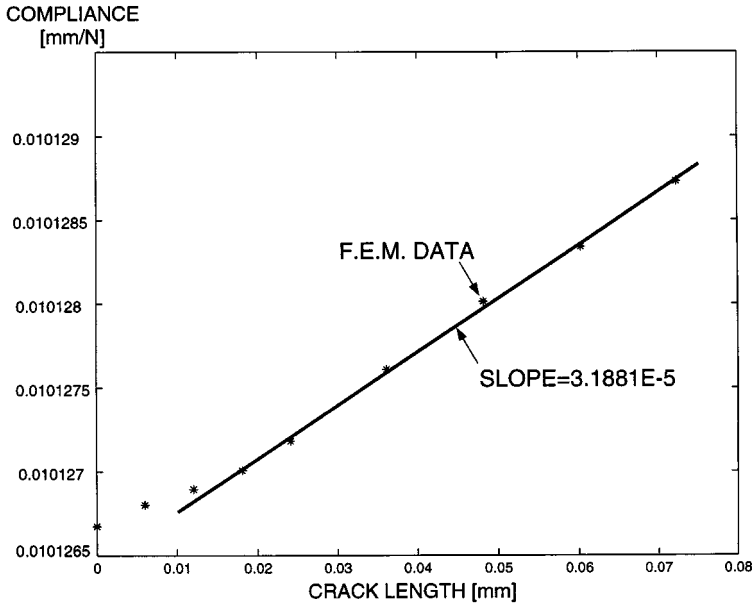

Figure 16. Compliance of a glass fiber composite ($V_f = 10$ percent) corresponding to the axisymmetric finite element model.

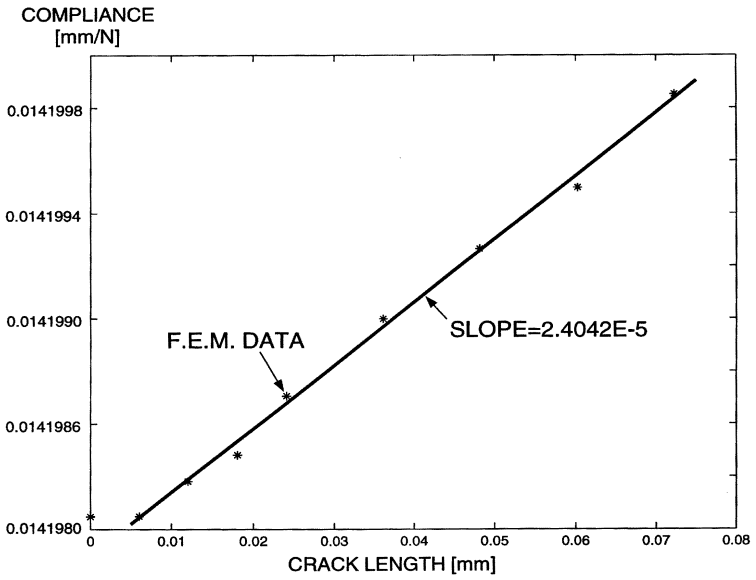

Figure 17. Compliance of a glass fiber composite ($V_f = 60$ percent) corresponding to the axisymmetric finite element model.

4. Finite element analysis of kink banding

The kink banding failure mode was simulated by employing the finite element method. The measured compressive stress-strain behavior of the resin has nonlinear characteristics. Observation under a microscope shows that the composite specimens possess geometric imperfections. The fibers in the composite are actually nonuniformly distributed. Also, fibers are

misaligned with respect to the loading axis, indicated by the angle of rotation ϕ with respect to the loading direction as indicated in Figure 7. We used the finite element method to simulate the experiments because such an approach enables modeling the measured nonlinear mechanical properties of the constituents and realistic geometric imperfections at least in a simplified way. The ABAQUS commercial finite element code was chosen for this study because of its capability to handle nonlinear problems.

4.1. FINITE ELEMENT MODEL

The composite specimen used in the compression test is of a circular cylindrical configuration with diameter 6.4 mm, overall length 63.5 mm and gage length 12.7 mm. To mesh the entire cylinder in a three-dimensional finite element model incorporating spatial inhomogeneity and fiber geometric imperfection is a difficult and time consuming task. Therefore, a small representative planar region (RPR) within the cylindrical specimen is modeled in a two-dimensional plane strain setting using the ABAQUS CPE4 element. Since the initial deformation field is uniform and homogeneous, working with a RPR enables the study of the salient features of the nonlinear aspects of this problem as will soon be evident. A recent study by Hsu, Vogler and Kyriakides (1998) who examined a particular uniformly packed three-dimensional model, revealed that three-dimensional corrections to the plane strain approximation were insignificant, at least for large volume fractions (50 percent). The plane strain approximation would incur the greatest departure from the intended physical situation at low volume fractions. However, it still provides insight into the deformation characteristics, which are commensurate with observed experimental data even at low volume fractions. This is especially true for the carbon fiber composites. Thus, at low volume fractions we expect qualitative agreement with experiment, while at higher volume fractions the results become more accurate.

In Figure 18, a finite element mesh corresponding to a glass fiber composite with $V_f = 10$ percent is shown. Dark areas correspond to fiber and lighter areas correspond to matrix. The element size is determined by the fiber diameter. Glass fibers have a diameter of 0.0241 mm, which is chosen as the height of one element (y-direction) for a glass fiber composite model. On the other hand, carbon fibers have a diameter of 0.005 mm and is also orthotropic. Two rows of elements are used to model the carbon fiber. The aspect ratio of an element is set to 2, and geometric initial imperfections are represented by a misalignment angle ϕ.

The material property of the matrix is measured from a compression test of the pure matrix specimen. The PLASTIC material card of ABAQUS allows us to simulate nonlinear material behavior modeled via a J2 incremental theory of plasticity. The essential ingredients of this theory are explained in numerous texts on plasticity. The plasticity theory used to model the matrix material and requisite justification is presented in Appendix A. Figure 19 shows the nonlinear compressive uniaxial stress-strain curve of the pure matrix, as measured via tests and as inputted into the ABAQUS code. The glass fiber is modeled as a linear elastic material. The material properties of the glass fiber used in this study are $E = 72$ GPa and $\nu = 0.35$. It is well known that carbon fiber is best described as an orthotropic material. However the orthotropic material properties of the carbon fiber are difficult to measure exactly. The following orthotropic properties which were obtained from several references (Guynn et al., 1992b; Jones, 1975; Kumar, 1991; Kumar et al., 1993; Kyriakides et al., 1995; Kyriakides and Ruff, 1997; Shu and Fleck, 1997) were used in this analysis.

$$E_{11} = 276\,\text{GPa},$$

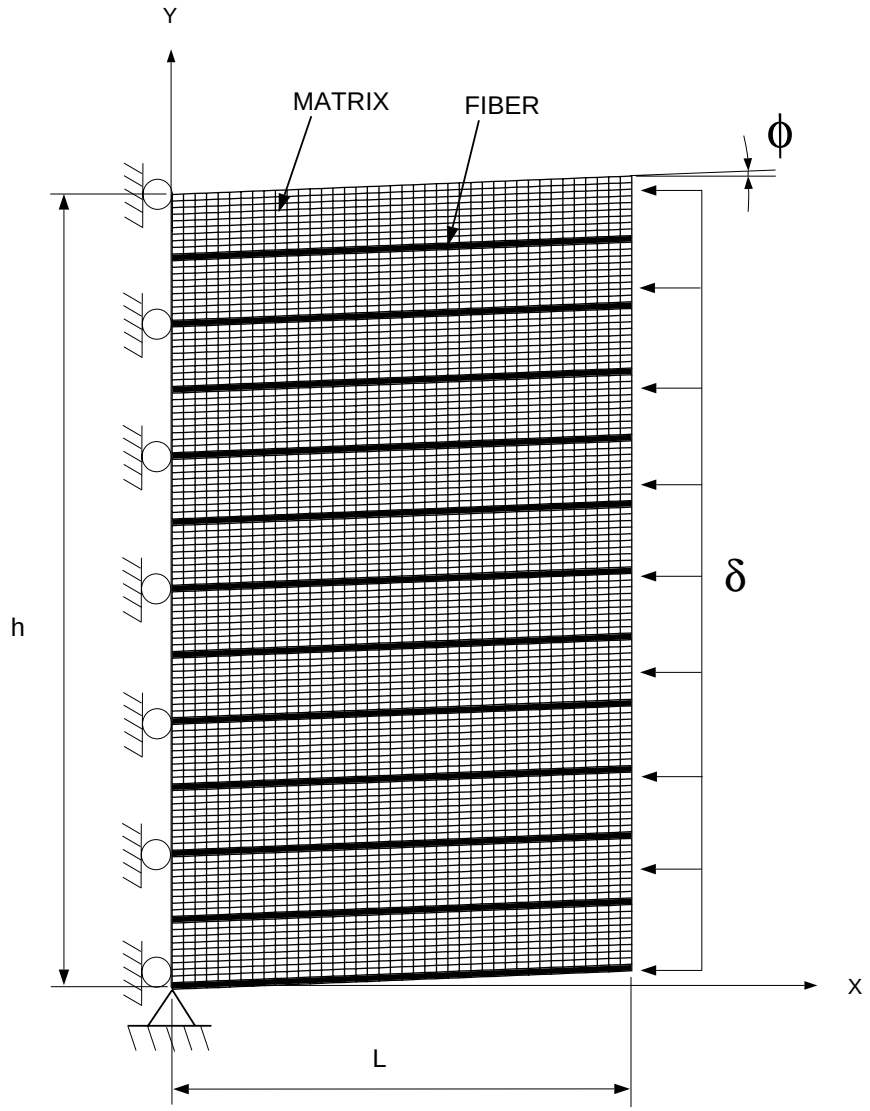

Figure 18. Uniform glass fiber finite element model ($V_f = 10$ percent).

$$E_{22} = E_{33} = 8760\,\text{MPa},$$
$$\nu_{12} = \nu_{13} = \nu_{23} = 0.35,$$
$$G_{12} = G_{13} = 12\,\text{GPa},$$
$$G_{23} = 3244\,\text{MPa}.$$

4.2. ANALYSIS

With reference to Figure 18, the right edge of the mesh is compressed uniformly in the x-direction by a prescribed displacement (δ) while the left edge of the mesh is constrained from moving in the x-direction. The left edge is free to move in the y-direction except the left bottom node which is constrained to prevent a rigid body motion. Using the RIKS method

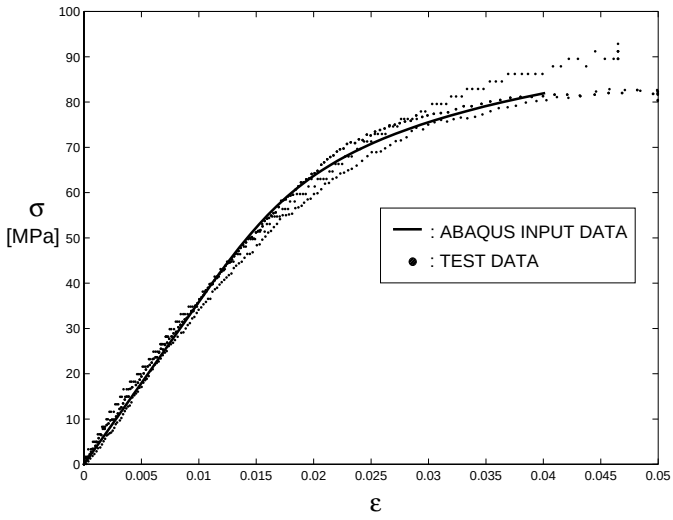

Figure 19. The uniaxial compressive stress-strain curve of the pure matrix.

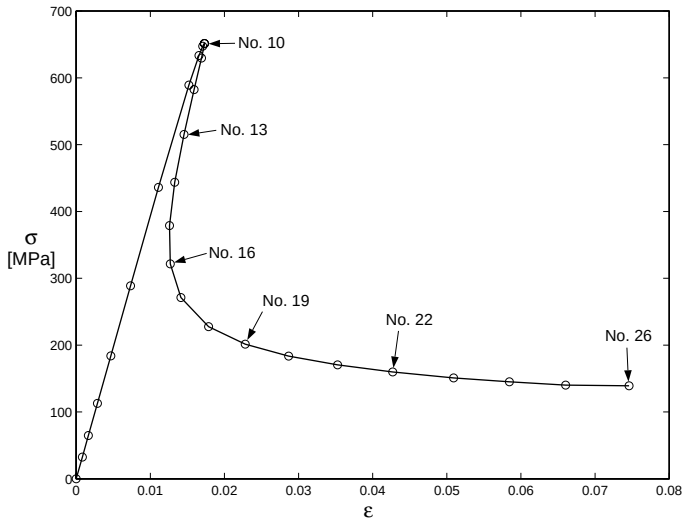

Figure 20. Typical σ–ε curve of a uniform glass fiber composite model, ($V_f = 50$ percent, $\phi = 2^\circ$).

supplied by ABAQUS, the reaction force resultant at the left edge can be computed for each increment of δ. From this data, the stress and strain values are calculated. Typical σ–ε curves from such an analysis are shown in Figure 20. Deformed geometries corresponding to each point marked in this figure are shown in Figure 21. The maximum stress (compressive strength of the composite) and stiffness of the composite can be obtained from this σ–ε curve.

Recall that when the specimens were observed under the optical microscope the fibers were nonuniformly distributed in the composite. To understand the effect of this spatial inhomogeneity on composite compressive strength, finite element models incorporating nonuniform fiber spacing were analyzed. Figure 22 shows a typical nonuniform glass fiber model used in the

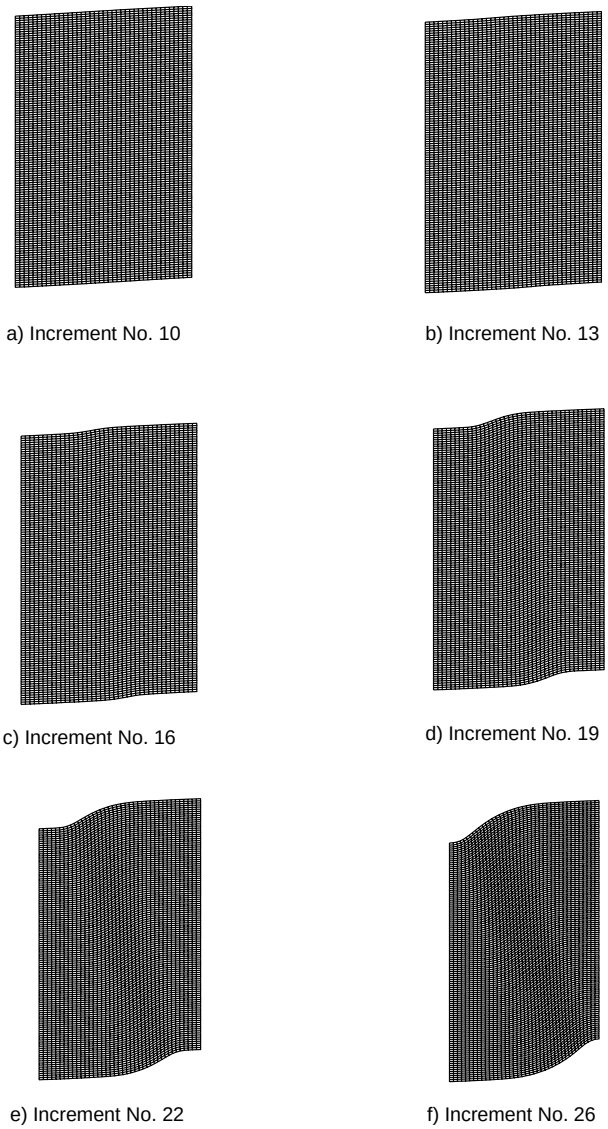

Figure 21. Typical deformed geometry of a uniform glass fiber composite model ($V_f = 50$ percent, $\phi = 2°$).

study. Fibers are located randomly inside the RPR while keeping the overall fiber volume fraction $V_f = 10, 20, 30, 40, 50$ and 60 percent, respectively. Two different nonuniform models were examined for $V_f = 40$ percent. The second nonuniform model for $V_f = 40$ percent has a more severe nonuniformity than the first nonuniform model. All 7 nonuniform models were assumed to have the same initial imperfection ($\phi = 2°$) and the same fiber properties (glass fiber), as used before.

4.3. Robustness of the F.E. model results

The results obtained via the finite element models described in the previous section were checked for accuracy and robustness in the following manner. These checks included dependence of results on element type, model size, element size and aspect ratio of model. Uniform

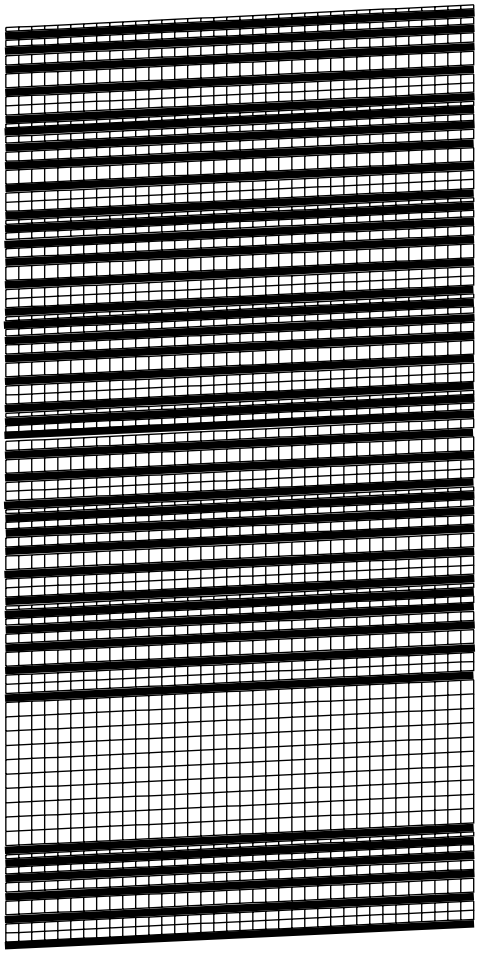

Figure 22. The finite element mesh for a nonuniformly spaced glass fiber model ($V_f = 40$ percent, $\phi = 2°$).

glass fiber models corresponding to the extreme cases of $V_f = 10, 60$ percent and $\phi = 2°$ were chosen as the candidates for the robustness study. Nonuniform glass fiber models and the nonuniform carbon fiber models were not examined in this manner because they include the same modeling features as with the uniform glass fiber models.

The CPE4 element (4-node bilinear plane strain quadrilateral element) was used to generate the previously presented results. The use of the CPE4 element is justified by comparing the analysis results using the CPE4 element models to the analysis results obtained via the use of the CPE8 element (8-node biquadratic plane strain quadrilateral element) model. For purposes of comparison, similar glass fiber composite models with CPE4 element and CPE8 element were examined. The first model used has dimensions of $L = 1.928\,\text{mm}$ and $h = 2.892\,\text{mm}$. The results obtained by using this model size is compared to the results of 'small' models with $L = 0.964\,\text{mm}$ and $h = 1.446\,\text{mm}$. Such an analysis examines the influence of overall mesh size and element type on the results obtained. Another model having a element size of $0.0241\,\text{mm} \times 0.0482\,\text{mm}$ produces results which are compared against results obtained with a model having an element size of $0.01405\,\text{mm} \times 0.0241\,\text{mm}$. Such a comparison establishes the effect of element size on the results obtained.

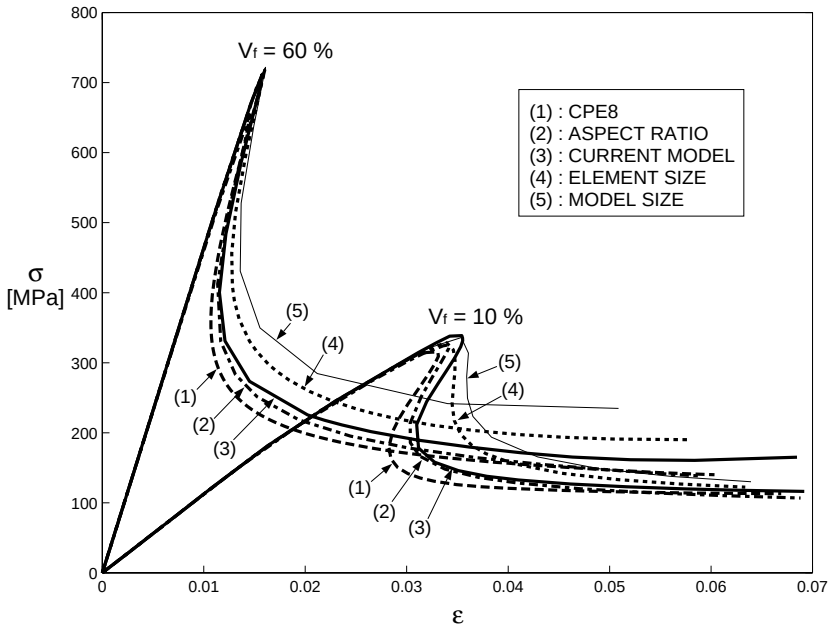

Figure 23. Verification of the numerical results obtained for glass fiber composites.

Comparison of the results obtained as described above revealed that the differences in maximum stresses between the models were $-7 \sim -0.9$ percent for $V_f = 10$ and $-7.3 \sim 1.4$ percent for $V_f = 60$ percent. These differences were deemed insignificant. The σ–ε curves predicted by the various finite element simulations are shown in Figure 23.

4.4. Discussion of finite element results

4.4.1. *Uniform glass fiber model*

All 12 uniform glass fiber models representing 6 fiber volume fractions ($V_f = 10 \sim 60$ percent) and 2 initial imperfections ($\phi = 2^\circ, 3^\circ$) were meshed and analyzed. Predictions of maximum stress and stiffness are shown in Table 2. As the fiber volume fraction increases, both the maximum stress and stiffness increase. As the initial imperfection increases, both of these quantities decrease. A typical σ–ε curve as shown in Figure 20 indicates that there is a sudden load drop after increment number 10. Corresponding deformed shapes shown in Figure 21 show a kink band geometry after the maximum stress point is reached. Initially the model compresses uniformly until the maximum stress point is reached. Immediately beyond this point, deformation localizes into a kink band with a corresponding load drop. The finite element simulations predict that all 6 fiber volume fraction models display a similar trend, i.e., a kink band appears in all of the models examined. However, in the experiment, only the high fiber volume fraction specimens ($V_f = 40 \sim 60$ percent) showed a distinct kink band (even then, splitting was noticeable) while low fiber volume fraction specimens ($V_f = 10 \sim 30$ percent) did not show kink banding. This difference in failure mode can be explained by revisiting the predictions of the splitting model presented earlier. When the uncompressed, as manufactured specimens were observed under the microscope, a measurable maximum initial imperfection of 3° was found. Hence, as shown in Figure 24, the analysis prediction of maximum stresses corresponding to $\phi = 2^\circ$ and $\phi = 3^\circ$ are compared against

Table 2. Results of finite element analysis for uniform glass fiber composites

V_f[%]		10.0	20.0	30.0	40.0	50.0	60.0
$\sigma_{\max}$	$\phi = 2^\circ$	338.8	457.5	537.3	589.6	651.5	712.3
[MPa]	$\phi = 3^\circ$	302.8	394.2	441.2	481.0	517.3	555.7
E_{11}	$\phi = 2^\circ$	11171	18172	25138	32104	39094	46160
[MPa]	$\phi = 3^\circ$	11034	17906	24671	31429	38244	45160

Table 3. Results of nonuniform glass fiber composite F.E. models.

V_f[%]	10.0	20.0	30.0	40.0	50.0	60.0
$\sigma_{\max}$[MPa]	335.7	454.0	540.8	599.6/585.8	653.5	719.2
E_{11}[MPa]	11191	18189	25217	32211/32199	39217	46310

the experimentally measured maximum strengths. While reasonable agreement between these numbers is present, the mode of failure observed in the experiment is clearly different and calls for a mechanism based model as presented earlier for axial splitting. In passing, it is noted that the influence of misalignment on the predicted axial stiffness (E_{11}) results in differences in the range $2.8 \sim 5.8$ percent for $\phi = 2^\circ$, and $0.5 \sim 4.5$ percent for $\phi = 3^\circ$ model.

4.4.2. *Nonuniformly spaced glass fiber models*

The analysis results of 7 nonuniformly spaced glass fiber models are listed in Table 3. All models have the same initial imperfection ($\phi = 2^\circ$) and same material properties. The predicted maximum stress of a nonuniformly spaced fiber model is slightly lower ($-0.7 \sim -0.9$ percent) than the corresponding uniformly spaced model in the low fiber volume fraction range ($V_f = 10,\ 20$ percent), while it is higher ($0.3 \sim 1.7$ percent) in the high fiber volume fraction range ($V_f = 30,\ 40,\ 50,\ 60$ percent) than the corresponding uniformly spaced glass fiber model. The second nonuniform model corresponding to $V_f = 40$ percent has a lower maximum stress value (-0.6 percent) than the corresponding uniform model. The axial stiffness of the composite E_{11} of the nonuniform model is slightly higher ($0.2 \sim 2.5$ percent) than the uniform model throughout the fiber volume fraction range examined. The trends of the response curves are similar to what was found for the corresponding cases of the uniformly spaced fiber models. Thus, the local nonuniform spacing of fibers do not appear to have a significant effect on the overall RPR response.

4.4.3. *Carbon fiber model*

Results corresponding to the carbon fiber simulations are summarized in Table 4. If we choose an initial imperfection $\phi = 4^\circ$ and $\phi = 5^\circ$ then, the predicted maximum stress and stiffness match up well with the test results as shown in Figure 25. Since the maximum measurable initial imperfection under a microscope was 3°, the 4° and 5° imperfections are regarded as larger than that found in practice. Just as in the glass fiber case, the predicted maximum stress and stiffness increases with increasing fiber volume fraction and show a corresponding decrease with increasing size of initial imperfection. A typical σ–ε curve and the corresponding deformed shapes are very similar to what was reported for the kinking analysis of the glass

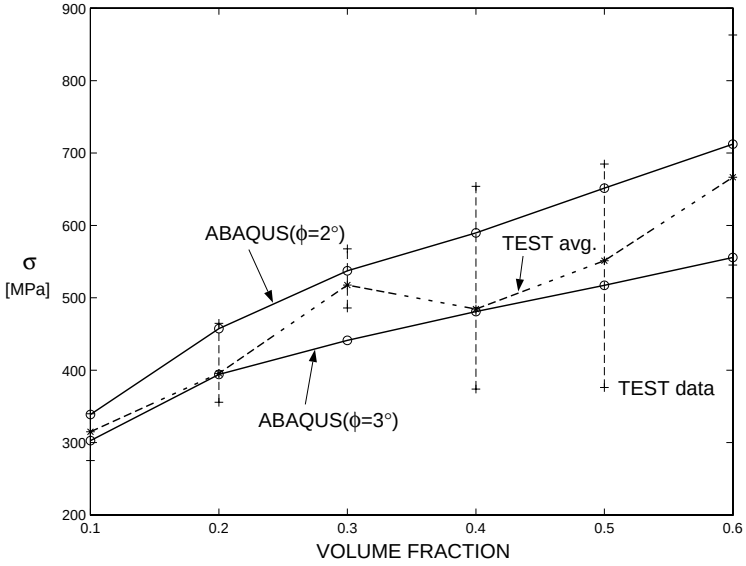

Figure 24. Predicted maximum stresses for glass fiber composites as a function of fiber volume fraction.

Table 4. Results of finite element analysis of carbon fiber composite F.E. models

V_f[%]		10.0	20.0	30.0	40.0	50.0	60.0
$\sigma_{\max}$	$\phi = 4°$	330.8	378.3	408.6	435.0	456.7	480.3
[MPa]	$\phi = 5°$	285.4	326.0	344.3	371.0	388.3	407.0
E_{11}	$\phi = 4°$	26889	47889	69252	89944	110667	135141
[MPa]	$\phi = 5°$	25000	43628	61389	79333	99233	119778

fiber composites. As before, the deformed shapes show a kink band after the maximum stress point is reached. Figure 26 shows a comparison between predicted results and test results for glass and carbon composites. The ABAQUS analysis results of carbon fiber composite specimens with $\phi = 2°$ show a higher maximum stress than the corresponding glass fiber model for the kink banding failure mode. Yet, the experimental results (which for glass fibers corresponds to splitting) show an opposite trend; the carbon fiber composites have *a lower maximum stress* than the glass fiber composite. As alluded to earlier in the discussion on splitting, carbon fiber composites show a favorable tendency to kink, whereas glass fiber composites are more prone to splitting. This fact is reflected in the model predictions that have been presented herein and these will be discussed next.

5. Discussion

Failure stresses for glass fiber composites predicted by the splitting model are seen to increase almost linearly with the increase of fiber volume fraction. As a result, they are lower than the test results in the low fiber volume fraction range and higher than the test results in the

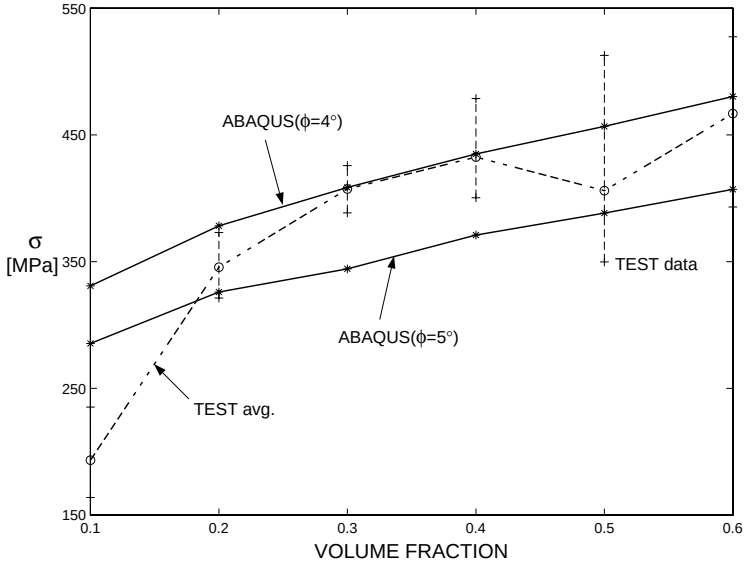

Figure 25. Predicted maximum stresses for carbon fiber composites as a function of fiber volume fraction.

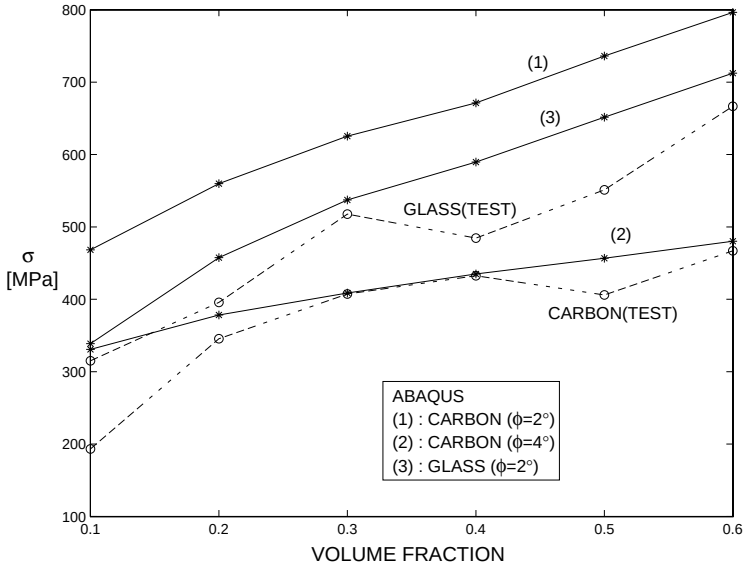

Figure 26. Compressive strength of glass and carbon fiber composites as a function of fiber volume fraction.

high fiber volume fraction range. The slopes of these curves are dictated mainly by the value of interfacial toughness γ_f the fiber radius, r_f and the fiber volume fraction, V_f. Predictions from the splitting model that include fiber misalignment were shown in Figure 13 and Figure 15, for the glass and carbon fiber composites respectively. A comparison between the experimental data and the predictions based on a range of interfacial toughnesses for a fixed value of misalignment angle showed that the splitting model was able to bound the compressive

failure stress in the fiber volume fraction range spanning 10–30 percent. For the carbon fiber composites the splitting model predictions show that very high axial compressive stresses are required to activate the splitting failure mode. The results show that glass fiber composites are favorably disposed to fail by splitting when compared with the carbon fiber composites. This finding also explains the dearth of photomicrographs in the literature on kinked glass fiber composites and the abundance of such photomicrographs for carbon fiber composites. The splitting model predictions also show that the splitting failure mode is favorable than the kink band failure mode for low fiber volume fractions, while the kink band failure mode is favorable than the splitting failure mode for high fiber volume fractions. Thus, when simultaneous splitting/kinking was seen in the high volume fraction glass composites, it is likely that the kinking event preceded splitting. Notice also that in the 30–40 percent fiber volume fraction range, a *failure mode transition* occurs in the glass fiber composites. Predictive results for carbon fiber composites obtained via the splitting model are compared to the test results in Figure 15. The splitting failure stresses are much higher than the test results throughout the entire fiber volume fraction range. Note that both the glass and carbon fiber systems were used as 'unsized' during the manufacturing process. Previous authors have stated that for the same matrix system, carbon usually has a higher γ_f than glass. Thus, even with the relatively small γ_f value used, the predicted splitting stresses for carbon fiber composites far exceed the test results, indicating the importance of the fiber modulus, fiber diameter and fiber volume fraction in influencing the *mechanism* of failure. As shown in Figure 26, the finite element results for the carbon fiber composites corresponding to kink banding were found to agree closely with the test results for an initial imperfection of $\phi = 4^\circ$. This mechanism of failure was clearly seen in the experimental results for carbon fiber composites as reported earlier.

6. Conclusions

Compressive response and failure characteristics of glass fiber and carbon fiber reinforced unidirectional composites have been examined experimentally. The carbon fiber composite was seen to have a lower compressive strength than the glass fiber composite, while the carbon fiber composite demonstrated a higher stiffness than the glass fiber composite. The difference in stiffness was explained via a simple rule of mixtures result while the difference in strength is due to the different mechanism of failure. Glass fiber composites demonstrated a splitting failure mode for low fiber volume fraction ($V_f = 10 \sim 30$ percent) and a combined splitting/kink banding failure mode for high fiber volume fraction ($V_f = 40 \sim 60$ percent). The carbon fiber composite demonstrated a kink band failure mode throughout the entire range of fiber volume fractions examined. An experimental study such as reported here, that examines how the various parameters in a composite influence unidirectional compressive strength is invaluable and broadens the scope of future investigations on composite compressive strength. We note here that the effect of ply thickness and the location of zero plies with respect to thickness on the compressive strength of multidirectional laminates are important and the interested reader is referred to Drapier et al. (1998) for more discussion on this aspect of composite compressive strength.

The analytical model for the splitting failure mode predicted that axial splitting failure is favorable for glass fiber composites at low fiber volume fractions. This model also showed that the ratio of axial moduli between fiber and matrix, the fiber diameter and the fiber volume fraction are just as important as the fiber/matrix interfacial fracture toughness towards dictat-

ing the mechanism of compressive failure. Furthermore, the kink banding model and the axial splitting model provide a means to assess the fiber volume fraction (for given constituents of a composite) at which the failure mechanism transitions between kink banding and splitting.

A two-dimensional finite element analysis of the kink banding failure mechanism showed that the maximum stress prediction for carbon fiber composites matched the test result with an initial imperfection $\phi = 4°$. The effect of nonuniform fiber volume fraction showed a negligible correction to the prediction with a uniform fiber volume fraction model. On the other hand, this same model was seen to provide reasonable agreement for the compressive strength of glass fiber composites at high volume fraction. To the best knowledge of the authors, this is the first instance in which a predictive capability that includes several competing mechanisms has been afforded to assess composite compressive strength.

Appendix A: Plastic material property of matrix

A compression test of the pure matrix specimen showed inelastic material behavior. A Coulomb torsion test of a pure matrix specimen is performed to obtain the shear stress-shear strain curve of the matrix material, which also exhibits inelastic behavior. There are two types of small strain volume preserving plasticity theories, J2 deformation theory and J2 incremental theory with isotropic hardening. The stress-strain curve obtained from the compression test of a pure matrix specimen is used to predict the shear stress-shear strain curve by using the two plasticity theories. The results are compared with the torsion experimental results.

A.1. Torsion test

A cylindrical shaped specimen of the vinyl ester matrix material with the same dimensions as used for the compression tests, was held by two grips at each end of the specimen. While one end was firmly held, the other end was rotated by a small measurable angle. A strain gage is attached at the center of the specimen at 45° with respect to the axial direction of the specimen. The shear stress-strain curve of the pure matrix is obtained from this torsion test as described in (Lyon, 1991). The test result is shown in Figure 27.

A.2. Deformation plasticity theory

When the uniaxial σ–ε curve of an elastic-plastic material is represented by the following Ramberg–Osgood equation

$$\varepsilon = \frac{\sigma}{E} + \left(\frac{\sigma}{B}\right)^n$$

where E : elastic modulus, B : constant, n : integer, then, according to J2 deformation theory, the shear stress-shear strain τ–γ curve can be reproduced by the following equation

$$\gamma = \frac{\tau}{G} + \left(\frac{\tau}{A}\right)^n$$

where G : elastic shear modulus, A : constant. The constants E, G, A and B can be shown to have the following relations

$$G = \frac{E}{2(1+\nu)},$$

$$A = \frac{B}{3^{1/2+1/2n}}$$

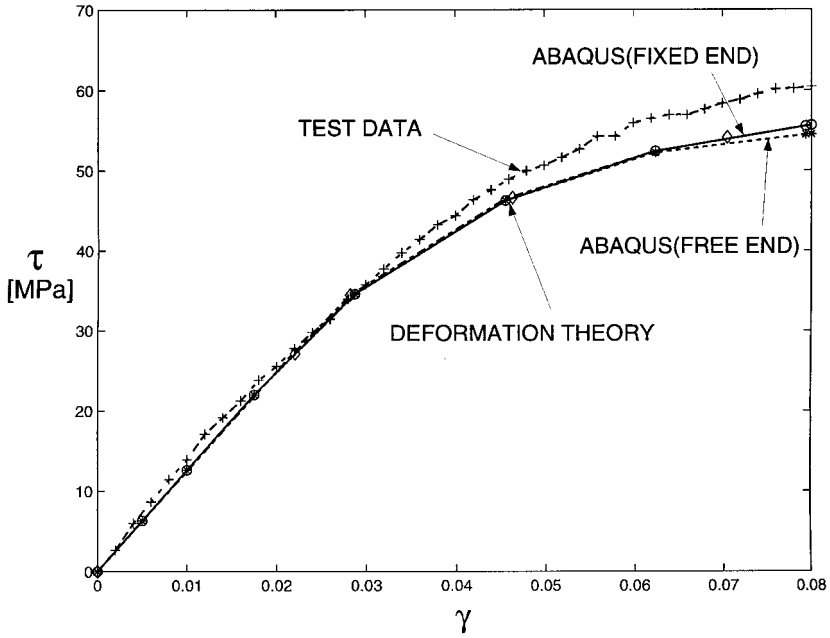

Figure 27. A comparison of the predicted and measured τ–γ curve of the matrix material.

where ν : Poisson's ratio.

At first, constants E, B and n are determined as $E = 3.6\,\text{GPa}$, $B = 0.136\,\text{GPa}$ and $n = 8$ from the σ–ε curve. Next, the constants G and A are determined as $G = 1.3\,\text{GPa}$ and $A = 0.073\,\text{GPa}$ by the above relations. Then the τ–γ curve should be the following

$$\gamma = \frac{\tau}{1.3} + \left(\frac{\tau}{0.073}\right)^8.$$

A.3. Incremental plasticity theory

The appropriateness of incremental plasticity theory is checked by using a finite element analysis via the ABAQUS commercial finite element code. A cylinder of 6.35 mm diameter and 40.64 mm length is modeled by 15-noded solid elements. The σ–ε data from the compression test is used as the input for the plastic material property of the finite element model. While one end of the cylinder model is fixed, the other end is rotated by a prescribed angle as is done in the test. The ABAQUS static analysis, which includes nonlinear geometry, calculates the torsional moment resultant at the fixed end. Two cases are considered in this analysis. First, the cylinder is under pure torsion with no restraint in the axial direction so the cylinder is free to change its length. Next, the cylinder is restrained from axial deformation. In the second case, the cylinder shows a slightly higher stiffness in the nonlinear region, which is due to the axial constraint that induces axial compression.

Comparison of all the results (deformation theory, incremental theory and test) are shown in Figure 27. This figure shows that the incremental plasticity theory and the deformation plasticity theory provide a reasonable model for the vinyl ester resin.

Appendix B: Axial compliance of a misaligned fiber

Consider the response of an axially loaded misaligned fiber of uniform cross sectional area, A_f, length $2l$ and elastic modulus E_f within the context of geometrically nonlinear Euler–Bernoulli planar(in the x- and z-plane) beam theory. Let a set of Cartesian coordinate axes be placed such that the x-axis is aligned with the load application direction and the z-axis perpendicular to it. Place the origin of the coordinate axes at $x = 0, z = 0$. Let the initial misalignment, total deflection in the z-direction measured from the fiber centerline and the additional deflection be denoted by $w_0(x)$, $w(x)$ and $w_1(x)$, respectively. Then, the deflection, $w(x) = w_0(x) + w_1(x)$, is governed by,

$$\frac{d^4w}{\mathrm{d}x^4} - \frac{d^4w_0}{\mathrm{d}x^4} + \lambda^2\frac{d^2w}{\mathrm{d}x^2} = 0$$

where, $\lambda^2 = P_f/E_f I_f$. Assuming an initial misalignment distribution of $w_0(x) = A_0(1 - \cos \pi x/2l)$, solving the above equation for clamped-clamped free to slide in the z-direction, boundary conditions imposed at $x = 0$ and $x = 2l$, respectively, and, adopting the definition of axial strain

$$\varepsilon_x = \frac{\mathrm{d}u}{\mathrm{d}x} + \frac{1}{2}\left(\frac{\mathrm{d}w}{\mathrm{d}x}\right)^2 - \frac{1}{2}\left(\frac{\mathrm{d}w_0}{\mathrm{d}x}\right)^2,$$

in conjunction with the one-dimensional stress-strain relation $\sigma_x = E_f\varepsilon_x$, we obtain the relation,

$$(EA)_{\text{eff}} = \frac{E_f A_f}{1 + \frac{A_0^2 A_f}{2I_f}}.$$

Acknowledgment

This paper is based, in part, on the PhD dissertation of the first author, submitted in April 1998, to the Department of Aerospace Engineering, University of Michigan, Ann Arbor. Parts of this paper were presented at the U.S. National Congress for Applied Mechanics, June 1998 and the American Society of Composites Meeting, September 1997. The authors are extremely grateful to the Army Research Office for supporting this research. Dr. Kailasam Iyer and Dr. Mohammed Zikry are the ARO scientific officers.

References

Ashby, M.F. (1992). *Engineering Materials I: An Introduction to their Properties and Applications*, Pergamon Press, New York.

Budiansky, B. and Fleck, N.A. (1993). Compressive failure of fiber composites. *Journal of the Mechanics and Physics of Solids* **41**, 183–211.

Camponeschi, E.T. Jr. (1991b). Compression of composite materials: A review. *Composite Materials: Fatigue and Fracture* (Third Volume) (Edited by T.K. O'Brien), ASTM STP 1110, American Society for Testing and Materials, Philadelphia, 550–578.

Chatterjee, S., Adams, D. and Oplinger, D.W. (1993). Test methods for composites a status report, Volume II. *Compression Test Methods*. U.S. Department of Transportation, Federal Aviation Administration Report DOT/FAA/CT-93/17.

Cherepanov, G.P. (1979). *Mechanics of Brittle Fracture*, McGraw-Hill, 688–692.

Cui, W.C., Wisnom, M.R. and Jones, M. (1992). A comparison of failure criteria to predict delamination of unidirectional glass/epoxy specimens waisted through the thickness. *Composites* **23**, 158–165.

Daniel, Isaac M., Hao-Ming, H. and Shi-Chang, W. (1996). Failure mechanisms in thick composites under compression loading. *Composites: Part B. Engineering* **27**, 543–552.

Drapier, S., Grandidier, J.-C. and Poitier-Ferry, M. (1998). A nonlinear numerical approach to the analysis of microbuckling. *Composites Science and Technology* **58**, 785–790.

Fleck, N.A. *Compressive Failure of Fiber Composites, Advances in Applied Mechanics*, Academic Press, New York, 33, 43–117.

Gibson, R.F. *Principles of Composite Material Mechanics*, McGraw-Hill, Inc.

Guynn, E.G., Ochoa, O.O. and Bradley, W.L. (1992a). A parametric study of variables that affect fiber microbuckling initiation in composite laminates: Part 1 – Analyses. *Journal of Composite Materials* **26**, 1594–1616.

Guynn, E.G., Ochoa, O.O. and Bradley, W.L. (1992b). A parametric study of variables that affect fiber microbuckling initiation in composite laminates: Part 2 – Experiments. *Journal of Composite Materials* **26**, 1617–1643.

Hercules Advanced Materials and Systems Company, Product Data-Carbon Fiber Type IM7.

Hsu, S.Y., Vogler, T.J. and Kyriakides, S. (1998). Compressive strength predictions for fiber composites. *Journal of Applied Mechanics* **65**, 7–16.

Jones, R.M. (1975). *Mechanics of Composite Materials*, Scripta Book Company, Washington, D.C.

Kawabata, S. (1990). Measurement of the transverse mechanical properties of high-performance fibers. *J. Text. Inst.* **81**(4), 432–447.

Kumar, S. (1991). Advances in high performance fibers. *Indian Journal of Fiber and Textile Research* **16**, 52–64.

Kumar, S., Anderson, D.P. and Crasto, A.S. (1993). Carbon fiber compressive strength and its dependence on structure and morphology. *Journal of Materials Science* **28**, 423–439.

Kyriakides, S., Arseculeratne, R., Perry, E.J. and Liechti, K.M. (1995). On the compressive failure of fiber reinforced composites, Proceedings of the sixtieth birthday celebration of Prof. W.G. Knauss. *International Journal of Solids and Structures* **32**(6/7), 689–738.

Kyriakides, S. and Ruff, A.E. (1997). Aspects of the failure and postfailure of fiber composites in compression. *Journal of Composite Materials* **31**(20), 2000–2037.

Lee, S.H. (1998). *Compressive Behavior of Fiber Reinforced Unidirectional Composites*, PhD thesis, Department of Aerospace Engineering, University of Michigan, Ann Arbor.

Lo, K.H. and Chim, E.S.-M. (1992). Compressive strength of unidirectional composites. *Journal of Reinforced Plastics and Composites* **11**, 838–896.

Lyon, Richard E. (1991). Shear strength of a ductile material from torsion of solid cylinders. *Journal of Testing and Evaluation*, **19**(3), 240–243.

Narayan, S. and Schadler, L. (1998). Private communication. Presentation at SES Meeting, September, Pullman, WA.

Peebles, L.H. (1995). *Carbon Fibers*, CRC Press.

Schapery, R.A. (1993). Compressive strength based on local buckling in viscoelastic composites. *Proceedings of the Third Pan American Congress on Applied Mechanics*, January.

Schapery, R.A. (1995). Prediction of compressive strength and kink bands in composites using a work potential. *International Journal of Solids and Structures* **32**(6/7), 739–765.

Schoeppner, G.A. and Sierakowski, R.L. (1990). A review of compression test methods for organic matrix composites. *Journal of Composites Technology and Research* **12**, 2–12.

Shu, J.Y. and Fleck, N.A. (1997). Microbuckle initiation in fiber composites under multiaxial loading. *Proceedings of the Royal Society of London, Series A* **453**, 2063–2083.

Sohi, M.M., Hahn, H.T. and Williams, J.G. (1987). *The Effect of Resin Toughness and Modulus on Compression Failure Modes of Quasi-Isotropic Graphite/Epoxy Laminates* (Edited by N.J. Johnston), Toughened Composites, ASTM STP 937, American Society for Testing and Materials, Philadelphia, 37–60.

Soutis, C., Fleck, N.A. and Smith, P.A. (1991). Failure prediction technique for compression loaded carbon fiber-epoxy laminate with open holes. *Journal of Composite Materials* **25**, 1476–1498.

Soutis, C., Berbinau, P., Goutas, P. and Curtis, P.T. (1998). Effect of off-axis ply orientation on 0° fiber microbuckling, submitted to *Composites A*.

Sun, C.T. and Jun, A.W. (1994). Compressive strength of unidirectional fiber composites with matrix nonlinearity. *Composites Science and Technology* **52**, 577–587.

Swanson, S.R. (1992). A micromechanics model for in-situ compression strength of fiber composite laminates. *Journal of Engineering Materials and Technology* **114**, 8–12.

Waas, A.M., Babcock, C.D. Jr. and Knauss, W.G. (1990). An experimental study of compression failure of fibrous laminated composites in the presence of stress gradients. *International Journal of Solids and Structures* **26**(9–10), 1071–1098.

Waas, A.M. and Schultheisz, C.R. (1995). Compressive failure of composites, Parts I and II. *Progress in Aerospace Sciences* **32**, 1–78.

Warner, S.B. (1995). *Fiber Science*, Prentice Hall.